Article | Received 26 June 2026; Revised 26 October 2026; Accepted 9 November 2026; Published 18 November 2026
https://doi.org/10.55092/sc20260022

# Study on dynamic compression properties of metakaolin-based geopolymer at different oyster shell powder substitution contents

**Peng Guo[1], Zhen Li[1], Yunhan Zhang[2], Laihuan Huang[1], Biao Lu[1] and Lifeng Fan[1,*]**

[1] College of Architecture and Civil Engineering, Beijing University of Technology, Beijing, China
[2] School of Civil and Environmental Engineering, Nanyang Technological University, Singapore, Singapore

* Correspondence author; E-mail: fanlifeng@bjut.edu.cn.

## Highlights:

- The feasibility of using oyster shell powder as material for geopolymers was studied.
- The dynamic mechanical properties of the geopolymers were analyzed.
- The optimum substitution rate of oyster shell powder in geopolymers was determined.

**Abstract:** The oyster shell powder (OSP) can substitute for the primary raw material in the geopolymer preparation process, and the substitution content has a significant effect on the mechanical properties of the geopolymer. This paper investigated the dynamic compression properties of metakaolin-based geopolymer at different OSP substitution contents. Firstly, metakaolin-based geopolymer specimens with OSP substitution rates ranging from 0% to 90% were prepared. Subsequently, the dynamic compression tests were performed on the specimens using a split Hopkinson pressure bar (SHPB) system. Finally, the failure mode of specimens during the dynamic compression process was analyzed by digital image correlation (DIC) technology. The findings indicated that as the OSP content increases, the dynamic compressive strength of the geopolymer first increases and then decreases. When the OSP substitution rate was 20%, the specimen reached its maximum strength, which is approximately 1.2 times that of the reference sample. The dissipated energy first decreases and then increases as the OSP content increases. When the OSP substitution rate was 20%, the dissipated energy of the specimen was lowest, which is approximately 0.7–0.9 times that of the reference sample. The dynamic compressive strength and dissipated energy of the specimens increase linearly with increasing impact pressure. Furthermore, DIC analysis revealed that the damage degree of the specimens first decreased and then increased as the OSP content increased.

**Keywords:** dynamic compression property; oyster shell powder; metakaolin-based geopolymer; split Hopkinson pressure bar; digital image correlation

Copyright©2026 by the authors. Published by ELSP. This work is licensed under Creative Commons Attribution 4.0 International License, which permits unrestricted use, distribution, and reproduction in any medium provided the original work is properly cited.

## 1. Introduction

Geopolymer is a building material that consists of an inorganic polymeric substance produced through the dissolution and subsequent polycondensation of aluminosilicate precursors in an alkaline medium [1]. This material exhibits excellent mechanical properties, which include high compressive strength, strong durability, and outstanding thermal stability. These characteristics make it a viable substitute for conventional cement-based mortars and concretes in building components [2,3]. Throughout their service period, geopolymer components are often subjected to dynamic loads, such as seismic and impact loads. Evaluating the structural integrity of buildings necessitates a thorough examination of geopolymer mechanical behaviour under dynamic loading conditions [4–6]. Therefore, it is important to investigate the dynamic mechanical characteristics of geopolymers.

The split Hopkinson pressure bar (SHPB) serves as a commonly used experimental device for evaluating material dynamic properties across strain rates from $10^2$ to $10^4$ $s^{-1}$ [7]. Previous studies have shown that geopolymers are strain rate dependent, with their strength, failure patterns, and energy absorption capacity changing markedly as strain rate varies [8–12]. The dynamic compressive behaviour of rubberized geopolymer concrete was investigated. The research revealed that the dynamic increase factor (DIF) rose significantly with increasing strain rate. Moreover, higher rubber content led to a greater enhancement of the DIF. The fragment size after specimen failure became smaller as the strain rate increased [13]. The crack propagation pathways in geopolymer concrete vary with strain rate was further studied. Under quasi-static or low-rate loading, cracks tend to develop mainly along the interfacial transition zone (ITZ) and the cementitious matrix. At high strain rates, cracks propagate through both the aggregates and the ITZ simultaneously. This mechanism involves greater energy absorption and clear rate-dependent failure features. Additionally, the rate sensitivity of geopolymer concrete depends on its strength level [14]. Low-strength geopolymer concrete tends to have higher dynamic strength enhancement factors and greater rate sensitivity than high-strength varieties [15]. These studies indicated that impact loads have a significant effect on the dynamic mechanical properties of geopolymers, and that the dynamic mechanical properties of geopolymers vary under different impact conditions.

In addition to impact conditions, different raw materials can also cause significant differences in the dynamic mechanical properties of geopolymer concrete [16–19]. It is important to study the dynamic mechanical properties of geopolymers with specific raw material systems. In aquaculture, oyster shells are a type of solid waste, primarily composed of calcium carbonate [20]. Studies have indicated that adding calcium-bearing substances can effectively modify the microstructure and properties of geopolymers [21–24]. The addition of calcium promotes the formation of C-S-H gel, which strengthens the geopolymer network and boosts compressive strength [25]. In addition, calcium salts affect the setting and rheological behaviour of fly-ash-based geopolymer pastes. This effect arises from a heterogeneous nucleation mechanism that accelerates early setting [26]. Moreover, adding 20% calcite to metakaolin geopolymer significantly increased its compressive strength. Nevertheless, excessive calcite could damage the gel network and reduce the available aluminosilicate content [27]. Currently, oyster shell is utilized in geopolymer technology in two main ways. One approach is to pulverize it into powder and use it as a calcium additive to replace part of the main raw material [28,29]. The effect of adding untreated oyster shell powder (OSP) to a slag-ceramic-powder-based geopolymer was investigated, aiming to evaluate how this combination affected high-temperature resistance. It was found that OSP incorporation

inhibited non-uniform shrinkage at high temperatures, thus improving compressive strength [30]. In previous experiments, OSP calcined at 800 °C was added to a pumice-based alkali-activated cement (AAC) geopolymer blend. The calcined OSP readily produced C-S-H gel under alkaline activation, greatly accelerating condensation and hardening. At a 50% addition level, the material strength rose by 20 MPa relative to the control group [31]. Carbonation and long-term durability are essential for geopolymers containing calcium-rich materials. Research indicated that during the carbonation-curing process, OSP promotes the carbonation of the material, leading to the formation of a large amount of carbonation products and reducing the overall porosity [32]. Regarding the influence of OSP on durability, although a denser and more uniform ITZ formed between oyster shell and geopolymer mortar, the oyster shells negatively affected the durability of the geopolymer [33]. Furthermore, alkali-activated waste seashell binder has been shown to reduce carbon emissions by approximately 60% compared with ordinary Portland cement (OPC) [34]. The other method is to crush oyster shells into graded particles for use as aggregates in geopolymer concrete [35,36]. Crushed oyster shells can also be used as a substitute for river sand in geopolymer production. Compared to river sand, the ITZ between oyster shells and mortar has a higher and more uniform density. Nevertheless, the high porosity of oyster shells negatively affects the mechanical properties, durability, and microstructure of the geopolymer [33]. Recent studies have demonstrated that metakaolin and natural calcium oxide can be used to produce geopolymers in a sustainable and cleaner process, highlighting the potential of calcium-containing materials in the development of environmentally friendly geopolymer materials [37]. Previous studies on OSP-modified geopolymers have mainly focused on quasi-static properties. Their dynamic response and failure mechanisms under high strain rates have not been comprehensively studied. The dynamic compressive behaviour of metakaolin-based geopolymer with OSP as a substitute material has not been analyzed. Therefore, it is important to further investigate the effect of OSP replacement content on the dynamic mechanical properties of geopolymers.

This study investigated the dynamic compressive behaviour of metakaolin-based geopolymer pastes with different OSP replacement ratios. Metakaolin was replaced by OSP at various ratios, producing eight groups of specimens with OSP contents of 0%, 10%, 20%, 30%, 40%, 60%, 80%, and 90%. SHPB tests were conducted under different impact pressures to obtain dynamic compressive strength, elastic modulus, and dissipated energy. A high-speed camera captured the failure process, and the failure modes were analyzed.

## 2. Materials and experimental methods

### *2.1. Materials*

The primary purpose of this study is to isolate and assess the effect of OSP, as a calcium-containing substitute material, on the dynamic compressive properties of the geopolymer, without the addition of aggregate. The primary materials employed in this study were metakaolin and OSP. The macroscale and microscale morphologies of these two materials are illustrated in Figure 1. As depicted in Figure 1a, metakaolin exhibits a brick-red appearance. The metakaolin utilized in this study was sourced from Henan Province, China, and was produced by calcining kaolin at 850 °C for 4.0 h. Figure 1b displays OSP, which has a rice-white colour. The oyster shells used in this experiment were obtained from Juxin Oyster Shell Factory in Yangxi County, Guangdong Province. OSP was prepared by pulverizing and

milling the cleaned oyster shells, followed by sieving to separate powder particles smaller than 74 μm. The alkaline activator was formulated by mixing NaOH flakes, sodium silicate solution, and water at a specified ratio. The NaOH had a purity exceeding 99.0 %, while the sodium silicate had a silicate modulus of 3.24.

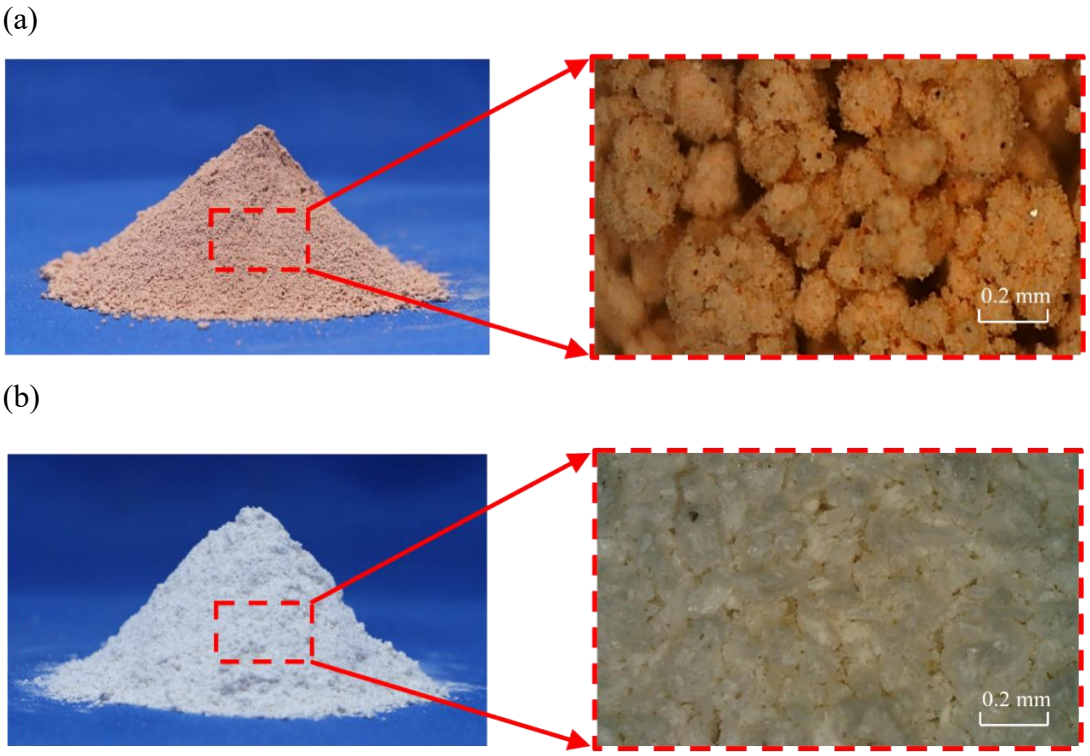



**Figure 1.** Macroscopic morphology and local details of metakaolin sample and OSP sample. **(a)** Metakaolin; **(b)** OSP.

The X-ray diffraction (XRD) patterns of metakaolin and OSP are presented in Figure 2. Metakaolin exhibits an amorphous aluminosilicate structure, characterized by a broad diffraction hump within the 2θ range of 20° to 30°, which is indicative of a highly reactive aluminosilicate pozzolanic material [38]. In contrast, the XRD profile of OSP reveals a crystalline nature, with distinct sharp peaks appearing near approximately 30° (2θ), and consists primarily of crystalline calcite ($CaCO_3$), indicating that OSP is a calcium-rich material.

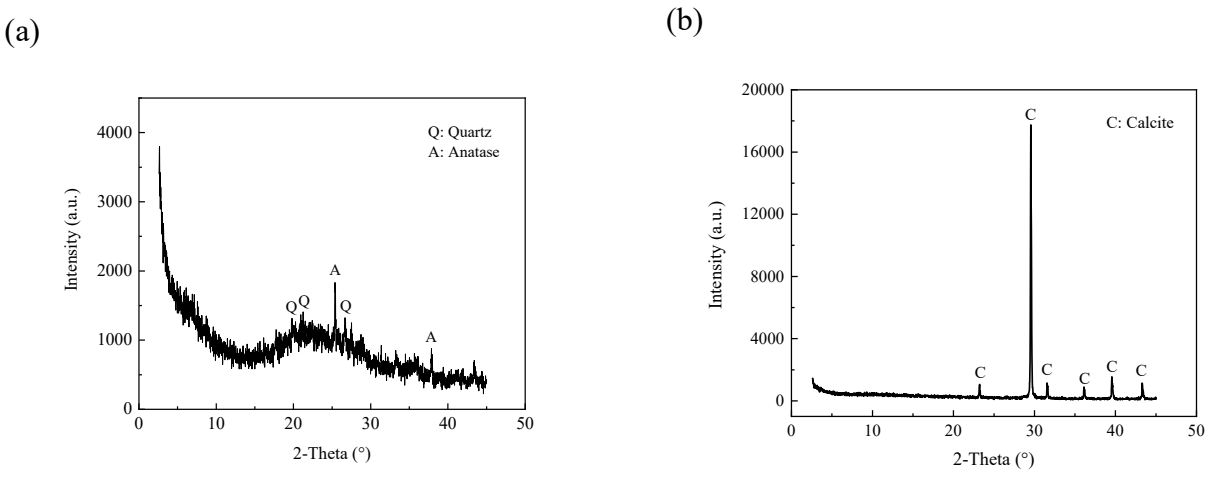



**Figure 2.** XRD pattern of metakaolin and OSP. **(a)** Metakaolin; **(b)** OSP.

*2.2. Preparation of the specimens*

This study aimed to investigate the dynamic compressive response of metakaolin-based geopolymers mixed with different OSP contents. Table 1 details the mixture formulations adopted. Based on the OSP substitution rates, the samples were split into eight sets, with OSP content of 0 %, 10 %, 20 %, 30 %, 40 %, 60 %, 80 %, and 90 %, respectively. The high OSP substitution rate of up to 90% was designed to more comprehensively investigate the reasonable range of OSP substitution rates. At this substitution rate, the content of reactive aluminosilicates in metakaolin decreases. However, the $CaCO_3$ in OSP is not inert in an alkaline medium and can participate in reactions to form calcium-containing gels. The production steps for the test specimens were as follows. Initially, an 8.0 M NaOH solution was made by dissolving solid NaOH flakes in a measured quantity of water. This alkaline solution was subsequently added to the $Na_2SiO_3$ solution to lower its modulus to 1.3. The activator was then mixed manually and left to cool down to room temperature. Next, metakaolin and OSP were blended in dry form for roughly 2.0 min to ensure uniformity. The alkaline activator was then progressively incorporated into the dry blend and mixed for approximately 4.0 min until a consistent, flowable paste formed. Afterwards, the fresh mixture was poured into moulds and subjected to vibration for 1.0 min to eliminate trapped air. The cast samples were then sealed with plastic sheeting and maintained at 20 °C with 95 % relative humidity for 24.0 h. Following demoulding, the specimens were kept under the same environmental conditions until the scheduled test date.

**Table 1.** Mix proportions of geopolymer with different OSP contents.

| OSP content (%) | Cementitious materials (kg/m$^3$) | | Alkaline activator solution (kg/m$^3$) | | |
|---|---|---|---|---|---|
| | Metakaolin | OSP | NaOH | $Na_2SiO_3$ | Water |
| 0 | 1320.53 | 0 | 82.55 | 499.47 | 257.98 |
| 10 | 1188.48 | 132.05 | 82.55 | 499.47 | 257.98 |
| 20 | 1056.42 | 264.11 | 82.55 | 499.47 | 257.98 |
| 30 | 924.37 | 396.16 | 82.55 | 499.47 | 257.98 |
| 40 | 792.32 | 528.21 | 82.55 | 499.47 | 257.98 |
| 60 | 528.21 | 792.32 | 82.55 | 499.47 | 257.98 |
| 80 | 264.11 | 1056.42 | 82.55 | 499.47 | 257.98 |
| 90 | 132.05 | 1188.48 | 82.55 | 499.47 | 257.98 |

All specimens were fabricated as cylinders measuring 50 mm in diameter and 25 mm in height. The height-to-diameter ratio was chosen as 0.5 to reduce any potential effects of axial inertia during impact loading [39]. After being cured under standard conditions for 28 days, the samples were taken from the curing chamber for SHPB measurements. Figure 3 shows a photograph of the prepared test blocks, revealing a clear correlation between block colour and OSP content: the blocks progressively transition from dark red to light red as the OSP percentage increases. Before testing, both end faces of each cylinder were ground to ensure surface smoothness and parallelism, with any deviation limited to within 0.02 mm. The experimental design comprised five different impact pressure levels and eight OSP dosages. For each condition, three replicate specimens were prepared to ensure data reproducibility.

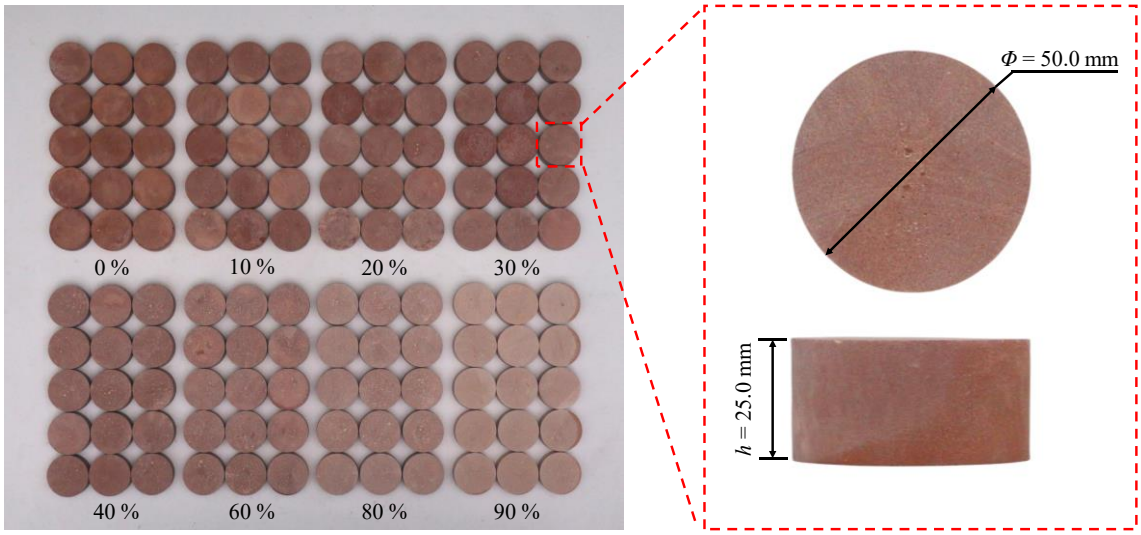



**Figure 3.** Morphology and dimensions of geopolymer specimens.

*2.3. Experimental methodology*

2.3.1. Split Hopkinson pressure bar test

SHPB experiments were performed to assess the dynamic compressive response of metakaolin-based geopolymer specimens incorporating different OSP ratios and subjected to various impact pressures. The testing device, depicted in Figure 4, features bars with a diameter of 50.0 mm. This equipment includes a striker pin, a velocity sensor, an air gun, a barrel, an incident bar, a transmission bar, and a shock absorber. All bars are fabricated from high-strength steel, exhibiting a Young's modulus of 200.0 GPa and a density of 7800.0 kg/m³. The incident and transmission bars are 1500.0 mm long, whereas the striker pin is 400.0 mm in length. The tapered profile of the striker pin assists in flattening the leading edge of the incident stress pulse, rendering it appropriate for testing brittle, non-uniform materials. Before each test, both contact faces of the specimen were coated with a thin Vaseline layer to reduce end friction [40].

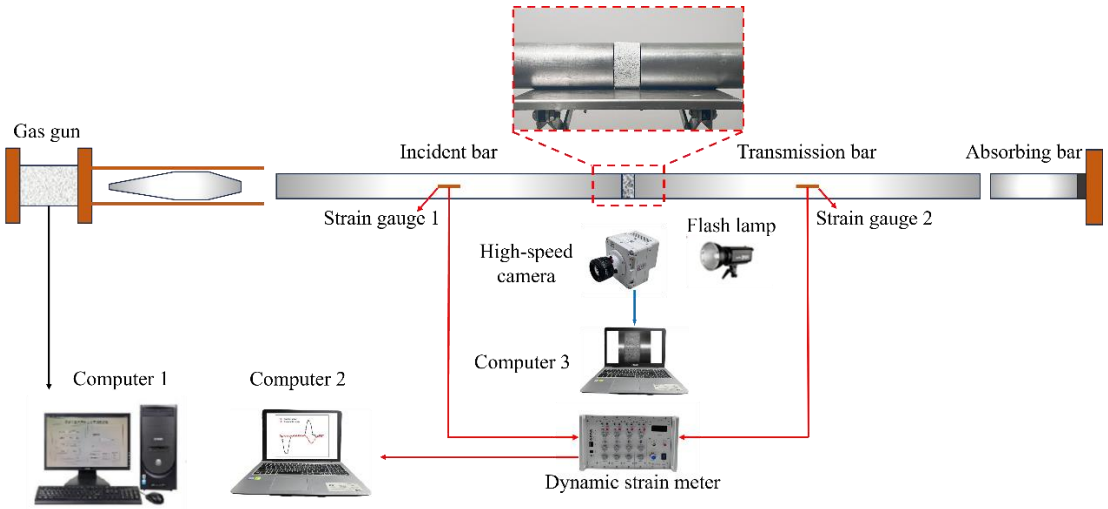



**Figure 4.** The SHPB system used in the dynamic compression test.

During operation, the air gun drives the striker pin to strike the incident bar, producing a half-sine compressive incident wave. Owing to the acoustic impedance mismatch at the specimen-bar boundaries,

the incident wave splits into transmitted and reflected components. Strain gauges mounted on the bars capture these signals, as shown in Figure 5a, which displays representative stress wave traces from a typical test. The dynamic forces are computed as follows:

$$F_1(t) = EA[\varepsilon_I(t) + \varepsilon_R(t)] \tag{1}$$

$$F_2(t) = EA\varepsilon_T(t) \tag{2}$$

where $F_1(t)$ is the force exerted on the left face of the specimen, and $F_2(t)$ is the force exerted on the right face. $E$ denotes the Young's modulus of the bar material, $A$ represents the cross-sectional area of the bar, and $\varepsilon_I$, $\varepsilon_R$ and $\varepsilon_T$ correspond to the incident, reflected, and transmitted strains, respectively.

A dynamic force equilibrium check was performed to validate the acquired data. Figure 5b shows the force histories from the dynamic compression test, confirming that the loads on the two specimen faces remained essentially equal over time. The average dynamic load is then given by [41]:

$$F(t) = \frac{F_1(t) + F_2(t)}{2} \tag{3}$$

where $F(t)$ is mean loading force.

In this SHPB test, five impact pressures were set at 0.25 MPa, 0.30 MPa, 0.35 MPa, 0.40 MPa, and 0.45 MPa, and at each impact pressure, specimens with eight different OSP replacement levels 0%, 10%, 20%, 30%, 40%, 60%, 80%, and 90% were tested. The specific test conditions are shown in Table 2.

(a) (b)

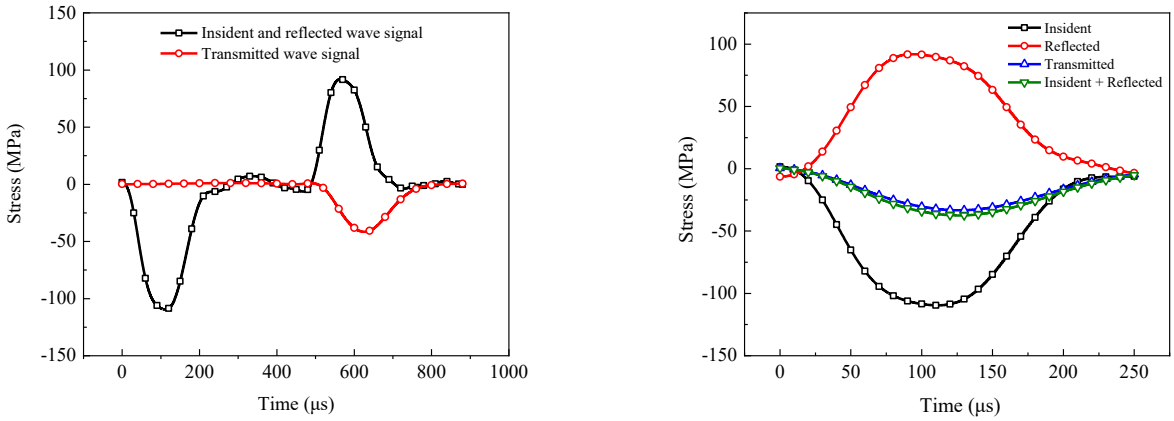



**Figure 5.** The incident waves, reflected waves, and transmitted waves in the SHPB test. **(a)** A typical stress wave signal recorded by strain gauges; **(b)** The dynamic stress equilibrium check.

**Table 2.** Dynamic strain rates of geopolymer specimens under different impact pressures and OSP contents.

| OSP content (%) | Dynamic strain rates ($s^{-1}$) | | | | |
|---|---|---|---|---|---|
| | 0.25 MPa | 0.30 MPa | 0.35 MPa | 0.40 MPa | 0.45 MPa |
| 0 | 121.3 | 143.1 | 159.7 | 175.4 | 198.6 |
| 10 | 106.6 | 125.7 | 140.3 | 154.1 | 174.5 |
| 20 | 79.9 | 94.3 | 105.3 | 115.6 | 130.9 |
| 30 | 83.8 | 98.8 | 110.3 | 121.1 | 137.1 |
| 40 | 87.9 | 103.8 | 115.8 | 127.2 | 144.0 |
| 60 | 92.6 | 109.2 | 121.9 | 133.9 | 151.6 |
| 80 | 103.5 | 122.1 | 136.3 | 149.7 | 169.5 |
| 90 | 146.5 | 172.8 | 192.9 | 211.8 | 239.9 |

2.3.2. High-speed photography system and DIC technology

In SHPB testing, a high-speed photography system and DIC technology are used to analyze specimen failure. The imaging setup consists of a high-speed camera (Phantom VEO 410 L) and an auxiliary spotlight. This camera operates at a frame rate of 50,000 frames per second with a resolution of 320 × 320 pixels. By combining the high-speed camera with DIC techniques, the complete compressive failure sequence of each specimen could be captured and analyzed. Before testing, a random speckle pattern was applied to the lateral surface of each specimen to facilitate subsequent image correlation processing [42].

## 3. Results and discussion

### *3.1. Dynamic compressive properties*

Figure 6 presents the dynamic stress-strain relationships of geopolymer specimens with various OSP substitution ratios under different impact pressures. These curves may be categorized into three distinct phases. In the initial elastic region, stress rises proportionally with strain. Following this, in the plastic regime, stress continues to climb as strain increases, albeit with a declining gradient. This behaviour indicates the onset of plastic deformation within the specimen, accompanied by progressive microcrack propagation and incipient material degradation. Once the stress attains its peak, it then plateaus at a relatively constant level while strain keeps increasing. Subsequently, as strain further increases, the stress progressively decreases, marking the final failure stage.

Figure 7 illustrates the variation of dynamic compressive strength of geopolymer with both impact pressure and OSP content. As Figure 7a shows, the compressive strength of geopolymers across all OSP levels exhibits a linear upward trend with rising impact pressure. The underlying reason is that elevated impact pressure delivers more impact energy to the specimen. Owing to the extremely short duration of the impact event, the specimen cannot absorb all this energy in time; consequently, the excess energy must be accommodated by increasing the load borne by the material. From Figure 7b, it is apparent that as the OSP content increases, the compressive strength first increases and later decreases, reaching its maximum at a 20 % OSP replacement. This trend is attributed to the combined effects of the calcium-containing OSP and the metakaolin-based binder matrix. The strength enhancement at moderate OSP contents may involve multiple mechanisms, including the filler effect of unreacted OSP particles reducing matrix porosity, the nucleation effect of $CaCO_3$ surfaces promoting gel formation, and the particle packing effect improving the packing density of the binder system.

Figure 8 displays the dynamic elastic modulus of the geopolymer at different impact pressures and OSP contents. The dynamic elastic modulus was determined from the slope of the linear elastic stage of the dynamic stress-strain curve. It was defined as the ratio of stress to strain at a specific stress level, such as one-half of the dynamic compressive strength. As seen in Figure 8a, the modulus rises linearly with impact pressure for all OSP levels. Figure 8b indicates that as OSP content grows, the modulus first ascends and then descends, reaching its maximum at 20 %. The trend in the dynamic elastic modulus as the OSP replacement content varies is consistent with that of the dynamic compressive strength. It can be seen that increases or decreases in strength and elastic modulus are primarily related to the OSP content. OSP affects the formation of the gel phase, the pore structure, and the densification of the matrix in geopolymer [43].

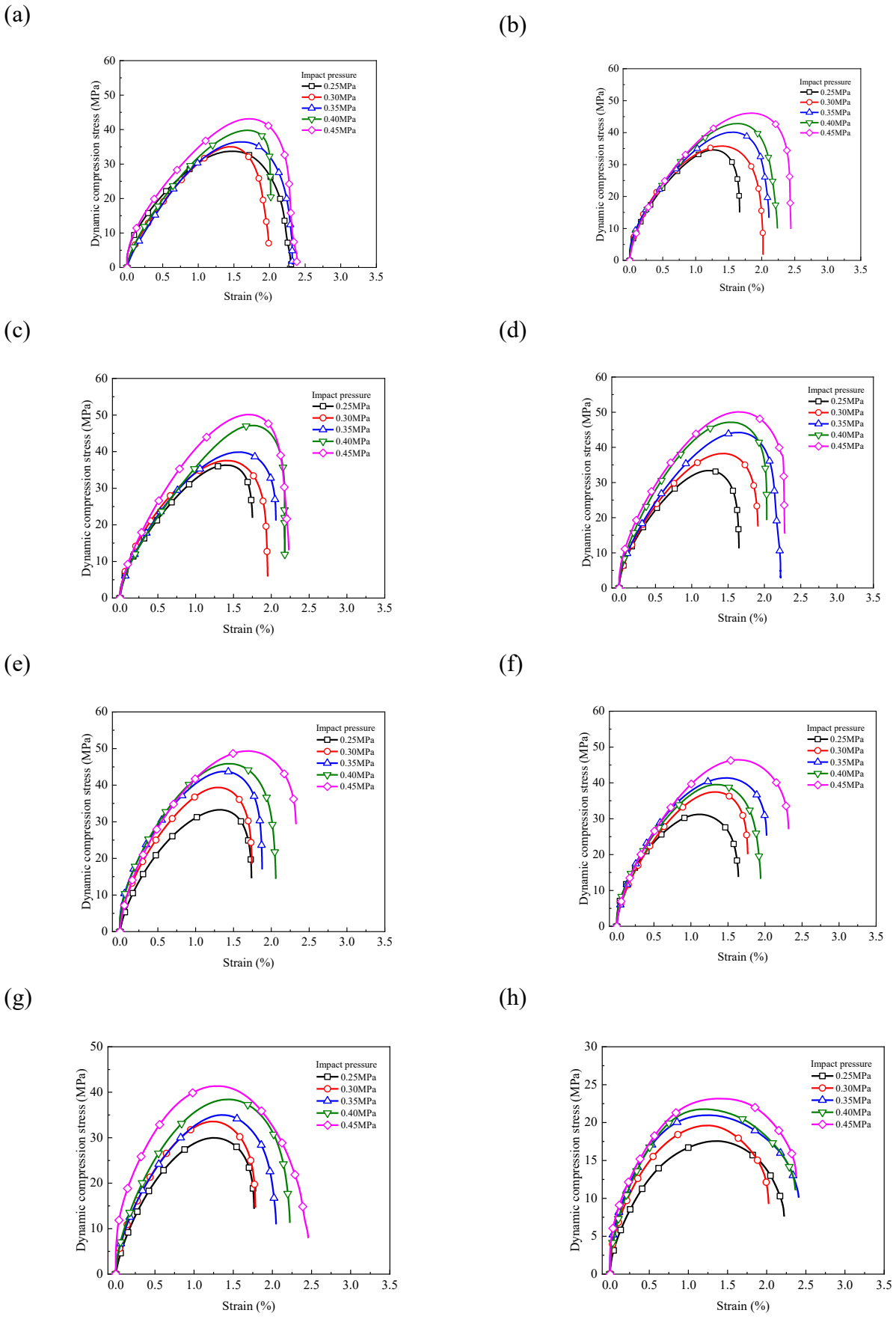



**Figure 6.** Dynamic compression stress-strain curves of different OSP contents. **(a)** 0%; **(b)** 10%; **(c)** 20%; **(d)** 30%; **(e)** 40%; **(f)** 60%; **(g)** 80%; **(h)** 90%.

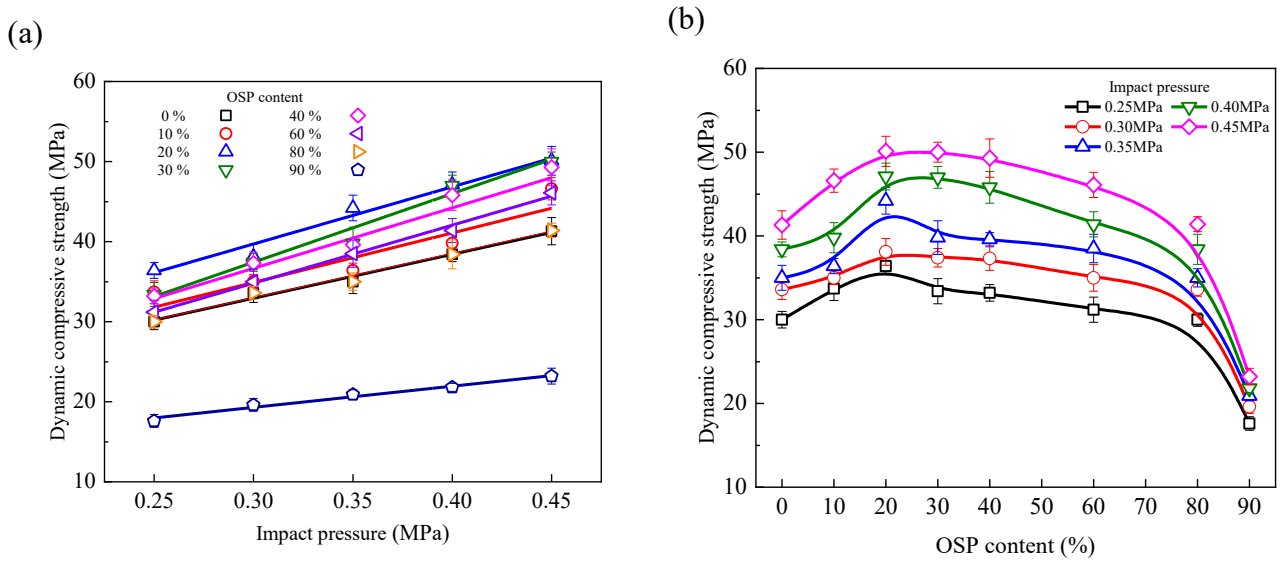



**Figure 7.** Dynamic compression strength of different impact pressure and OSP contents. **(a)** Impact pressure; **(b)** OSP content.

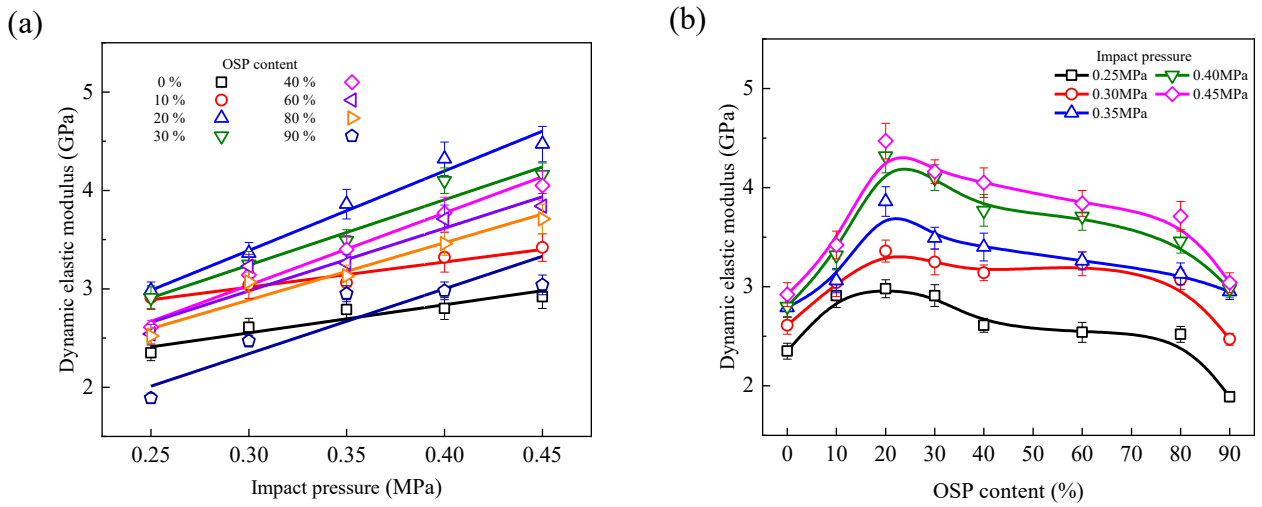



**Figure 8.** Dynamic elastic modulus of different impact pressure and OSP contents. **(a)** Impact pressure; **(b)** OSP content.

### *3.2. Energy dissipation*

During SHPB testing, the specimen undergoes energy conversion and transmission throughout the entire process from deformation to eventual failure. Based on the principle of energy conservation, the following relationship holds:

$$W_I = W_R + W_T + W_D \tag{4}$$

where $W_I$, $W_R$ and $W_T$ denote the incident, reflected, and transmitted energies, respectively. These energies can be determined using the following expressions [44]

$$W_I(t) = (AC/E)\int_0^\tau \sigma_I^2(t)\ \mathrm{d(t)} \tag{5}$$

$$W_R(t) = (AC/E)\int_0^\tau \sigma_R^2(t)\ \mathrm{d(t)} \tag{6}$$

$$W_T(t) = (AC/E)\int_0^{\tau} \sigma_T{}^2(t)\ \mathrm{d(t)} \tag{7}$$

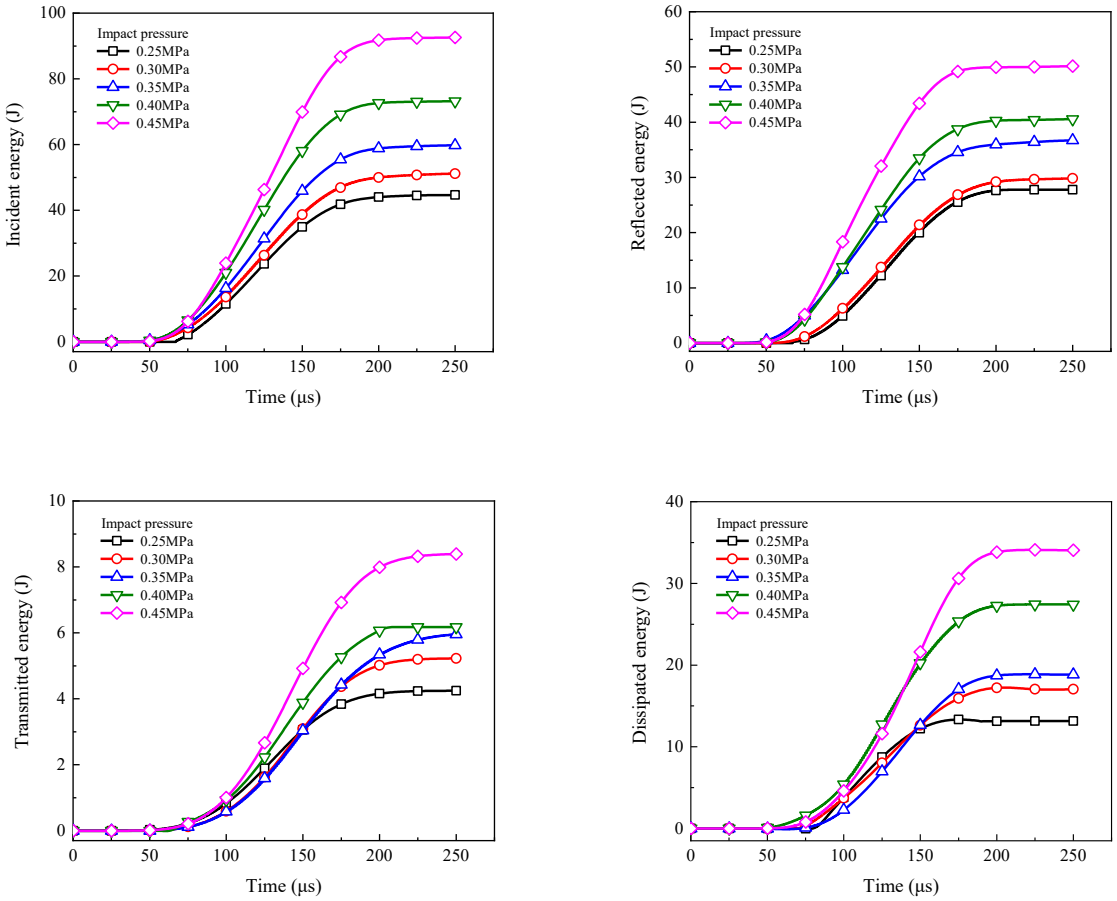
where $\sigma_I(t)$, $\sigma_R(t)$, and $\sigma_T(t)$ represent the incident, reflected, and transmitted stresses, respectively. The parameters $A$, $C$ and $E$ correspond to the cross-sectional area, wave velocity, and Young's modulus of the steel bars. Once the specimen absorbs the incident energy, the majority is consumed in generating and propagating cracks, while a minor portion is dissipated as other forms, such as thermal or acoustic energy. Provided that energy losses at the specimen-bar interfaces are neglected, the dissipated energy can be derived from the conservation law as:

$$W_D = W_I - W_R - W_T \tag{8}$$

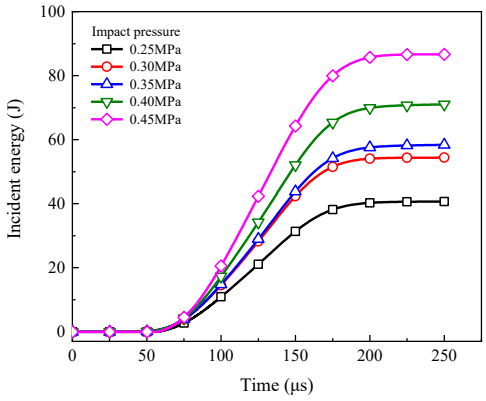
where $W_D$ denotes dissipation energy.

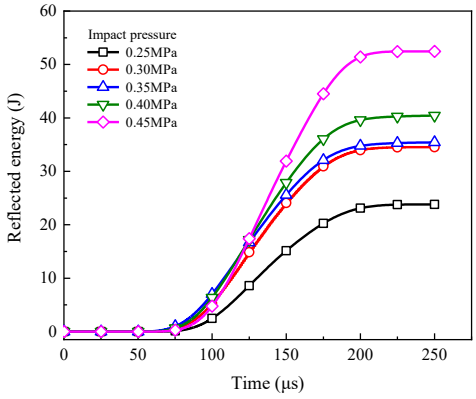
Figure 9 illustrates the changes in the four energy components under dynamic loading. As observed in Figure 9, all curves exhibit a gradual upward trend initially, followed by a sharp rise, and eventually level off. This progression can be generally divided into three phases, densification, linear ascent, and plateau. During the densification phase, the curve slope remains relatively flat due to the limited energy demand. In the linear ascent phase, the absorbed energy is utilized to compact existing microcracks and initiate new ones, with the energy curve rising steadily over time and dissipated energy increasing rapidly. In the plateau phase, the energy curve stays nearly flat, indicating that the specimen has already fractured and can no longer absorb additional energy.

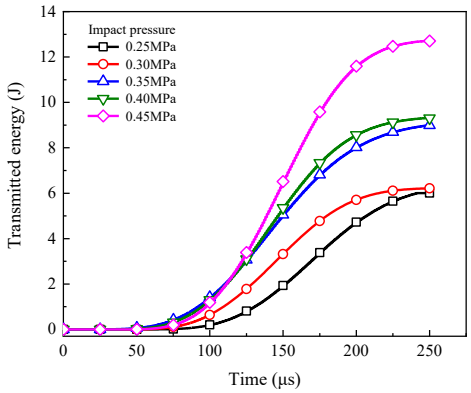
(a)

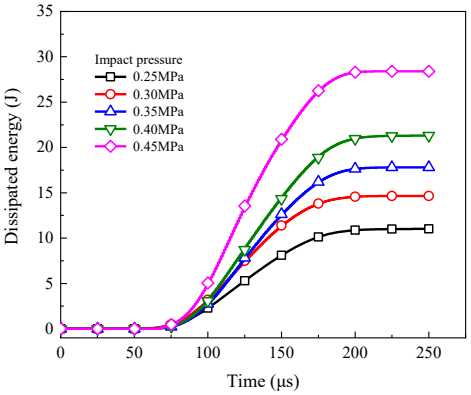


(b)

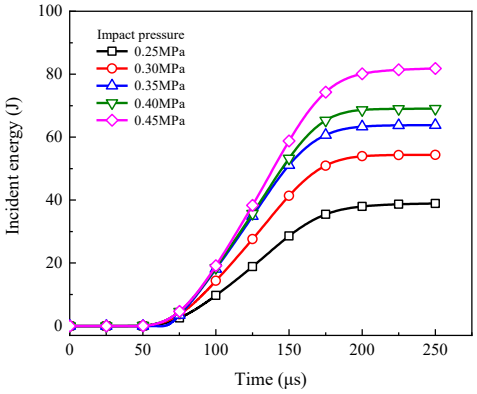

Impact pressure
0.25MPa
0.30MPa
0.35MPa
0.40MPa
0.45MPa
Incident energy (J)
Time (μs)

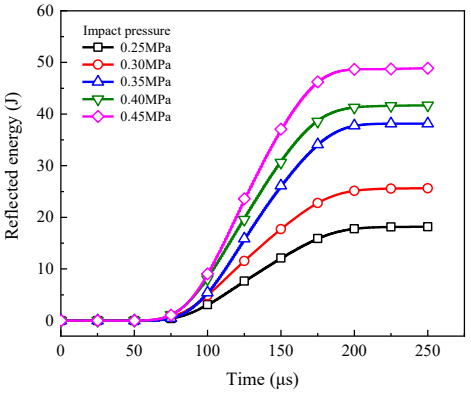

Impact pressure
0.25MPa
0.30MPa
0.35MPa
0.40MPa
0.45MPa
Reflected energy (J)
Time (μs)

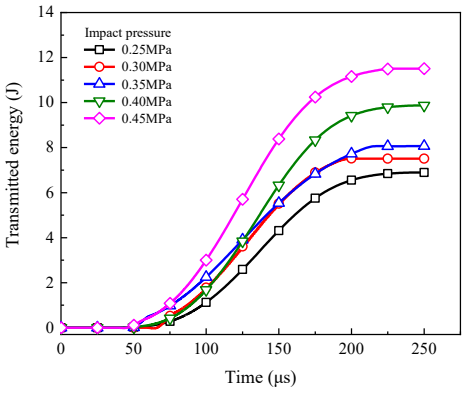

Impact pressure
0.25MPa
0.30MPa
0.35MPa
0.40MPa
0.45MPa
Transmitted energy (J)
Time (μs)

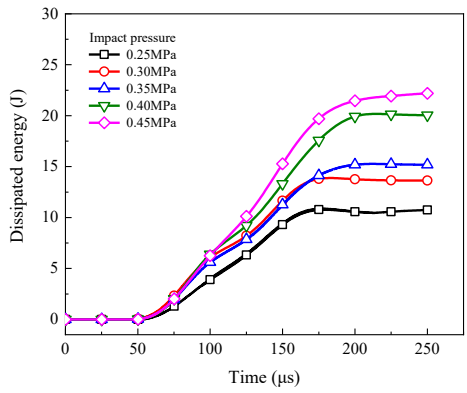

Impact pressure
0.25MPa
0.30MPa
0.35MPa
0.40MPa
0.45MPa
Dissipated energy (J)
Time (μs)

(c)

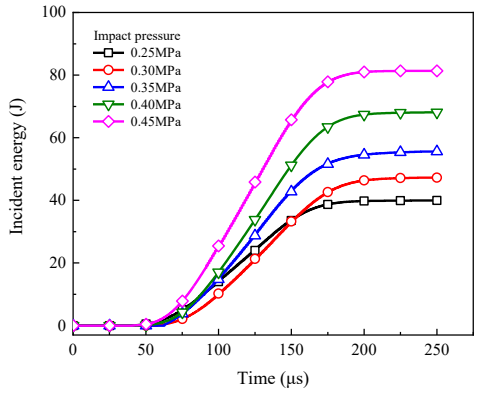

Impact pressure
0.25MPa
0.30MPa
0.35MPa
0.40MPa
0.45MPa
Incident energy (J)
Time (μs)

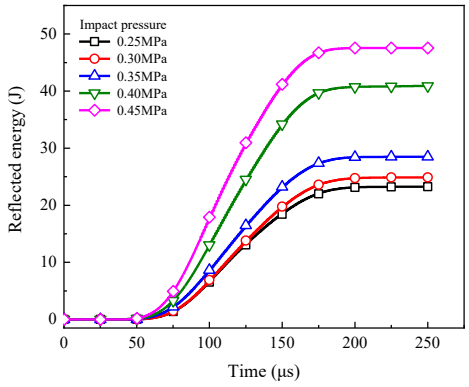

Impact pressure
0.25MPa
0.30MPa
0.35MPa
0.40MPa
0.45MPa
Reflected energy (J)
Time (μs)

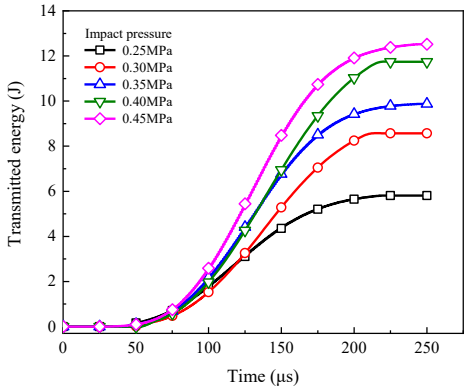

Impact pressure
0.25MPa
0.30MPa
0.35MPa
0.40MPa
0.45MPa
Transmitted energy (J)
Time (μs)

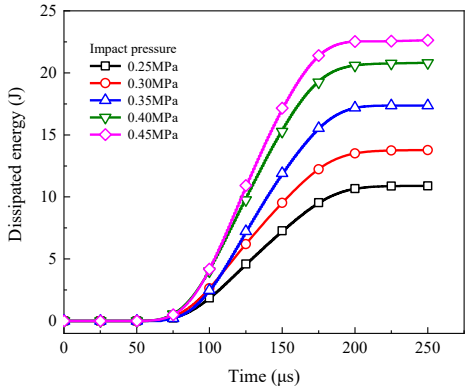

Impact pressure
0.25MPa
0.30MPa
0.35MPa
0.40MPa
0.45MPa
Dissipated energy (J)
Time (μs)

(d)

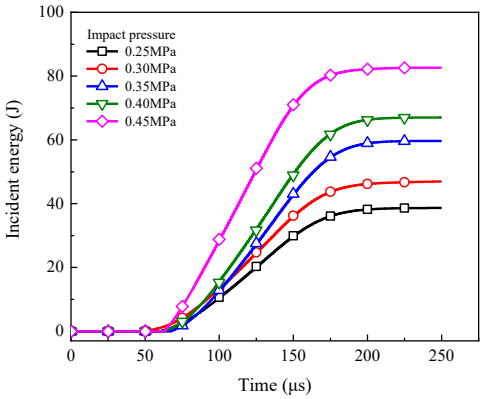

Impact pressure
0.25MPa
0.30MPa
0.35MPa
0.40MPa
0.45MPa
Incident energy (J)
Time (μs)

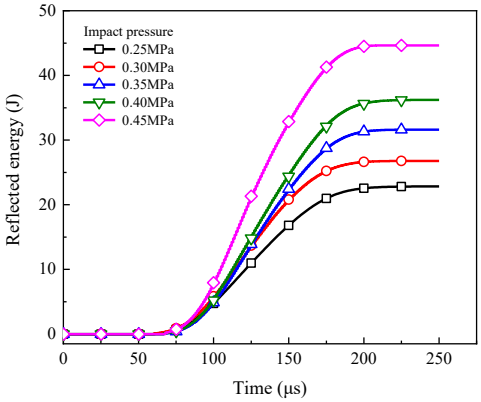

Impact pressure
0.25MPa
0.30MPa
0.35MPa
0.40MPa
0.45MPa
Reflected energy (J)
Time (μs)

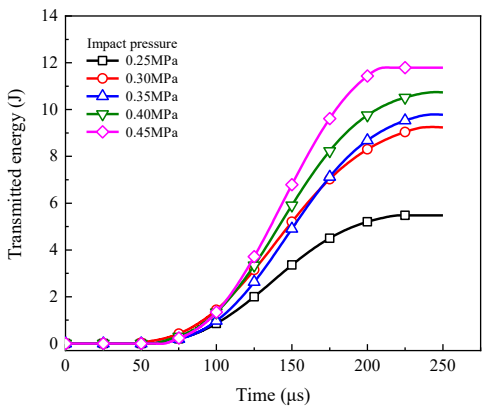

Impact pressure
0.25MPa
0.30MPa
0.35MPa
0.40MPa
0.45MPa
Transmitted energy (J)
Time (μs)

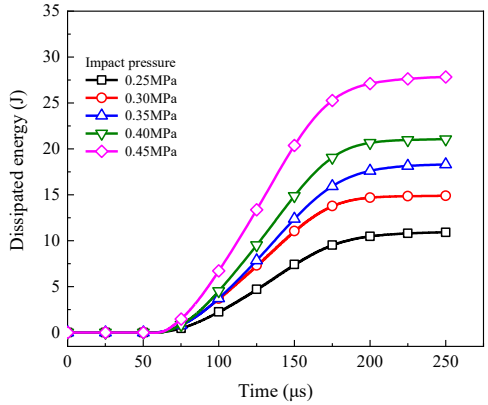

Impact pressure
0.25MPa
0.30MPa
0.35MPa
0.40MPa
0.45MPa
Dissipated energy (J)
Time (μs)

(e)

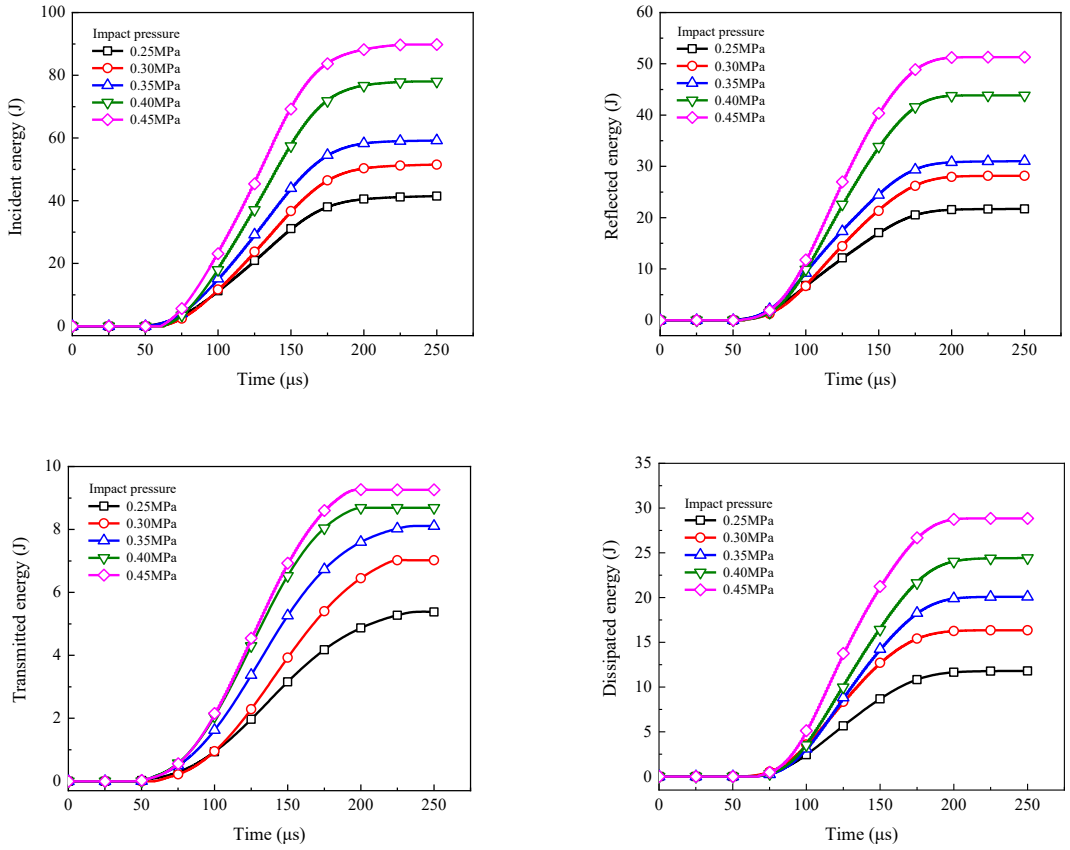

Impact pressure
0.25MPa
0.30MPa
0.35MPa
0.40MPa
0.45MPa
Incident energy (J)
Time (μs)


Impact pressure
0.25MPa
0.30MPa
0.35MPa
0.40MPa
0.45MPa
Reflected energy (J)
Time (μs)

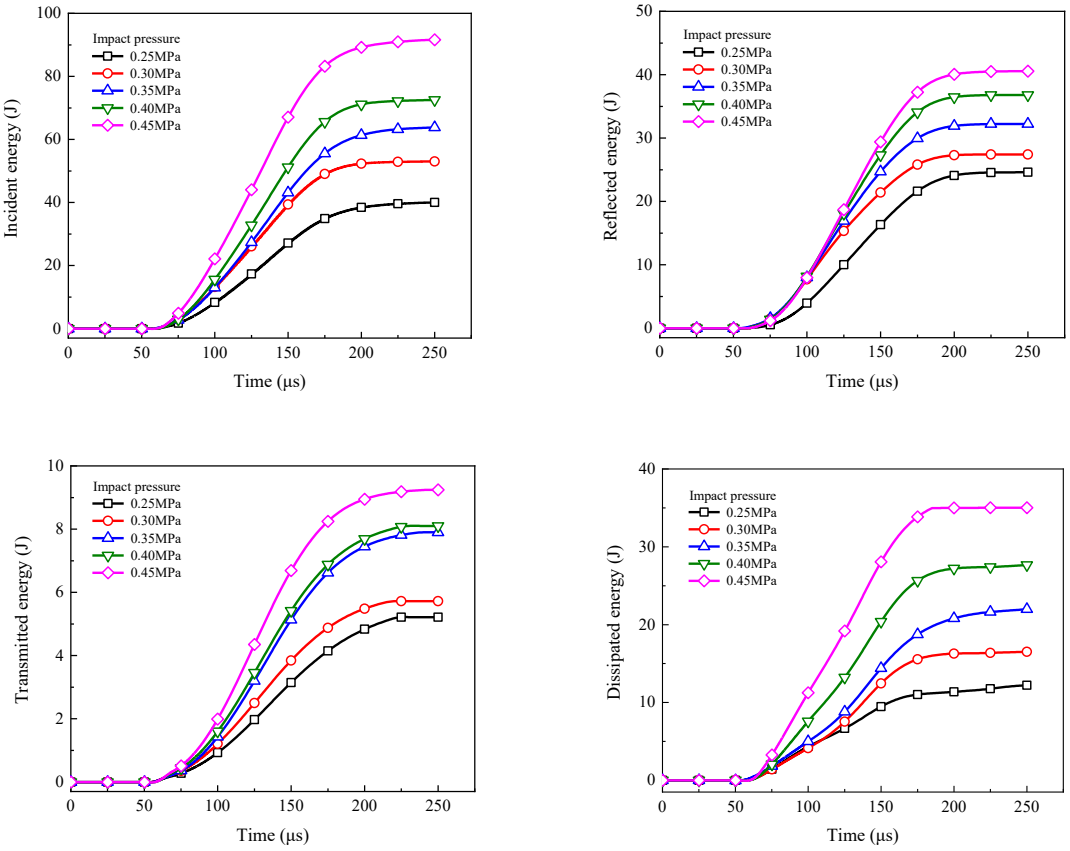

Impact pressure
0.25MPa
0.30MPa
0.35MPa
0.40MPa
0.45MPa
Transmitted energy (J)
Time (μs)


Impact pressure
0.25MPa
0.30MPa
0.35MPa
0.40MPa
0.45MPa
Dissipated energy (J)
Time (μs)

(f)


Impact pressure
0.25MPa
0.30MPa
0.35MPa
0.40MPa
0.45MPa
Incident energy (J)
Reflected energy (J)
Transmitted energy (J)
Dissipated energy (J)
Time (μs)

(g)


Impact pressure
0.25MPa
0.30MPa
0.35MPa
0.40MPa
0.45MPa
Incident energy (J)
Reflected energy (J)
Transmitted energy (J)
Dissipated energy (J)
Time (μs)

(h)

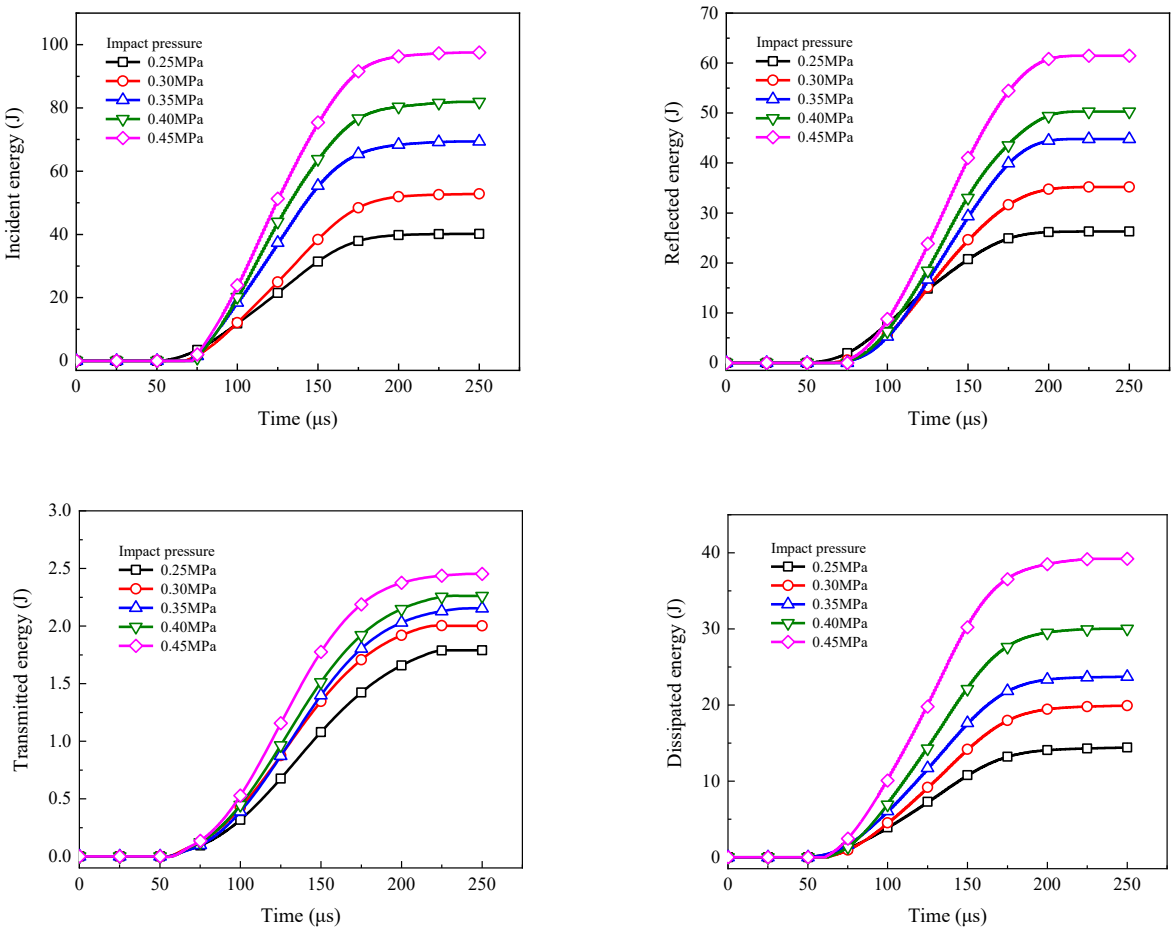



**Figure 9.** Dynamic energy curves of different OSP contents. **(a)** 0%; **(b)** 10%; **(c)** 20%; **(d)** 30%; **(e)** 40%; **(f)** 60%; **(g)** 80%; **(h)** 90%.

Figure 10 illustrates the variation in dissipated energy for the specimens. Figure 10a depicts the relationship between dissipated energy and impact pressure. It is evident that for all OSP contents, the dissipated energy rises linearly with increasing impact pressure. Figure 10b presents the effect of dissipated energy on OSP content. As the OSP content increases from 0 % to 20 %, the dissipated energy gradually declines. Conversely, when the OSP content rises from 20 % to 90 %, the dissipated energy progressively increases. This trend can be ascribed to the fact that the incorporation of a small amount of OSP raises the brittleness of metakaolin-based geopolymer. Under impact loading, the specimen cannot undergo sufficient plastic deformation and instead undergoes brittle fracture directly, thereby leading to lower dissipated energy.

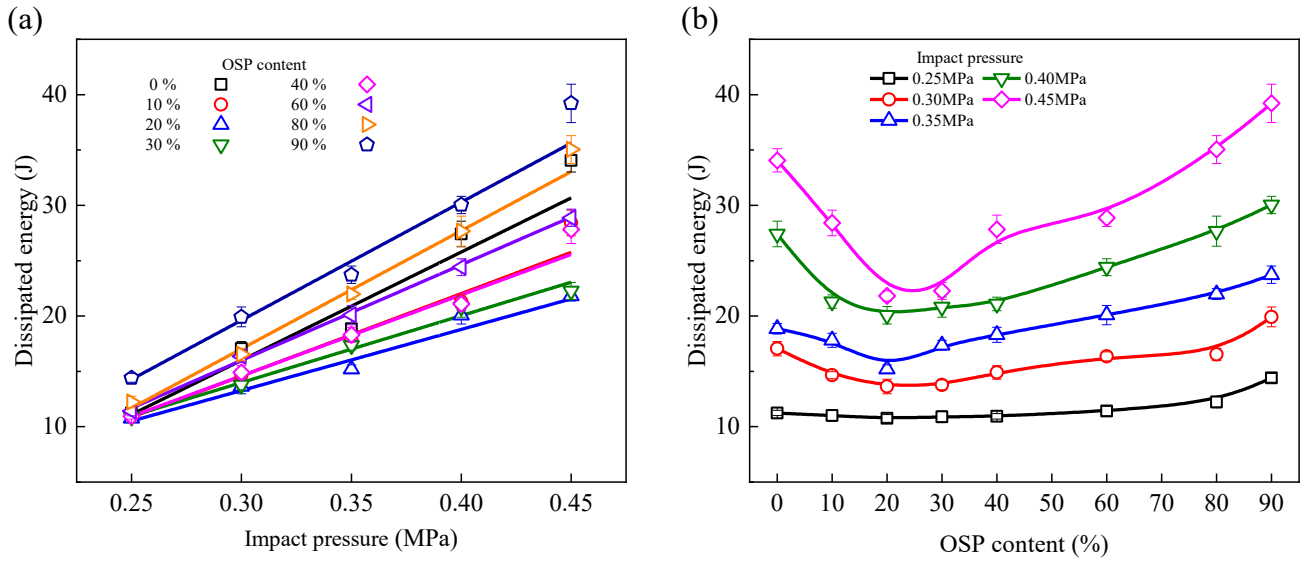
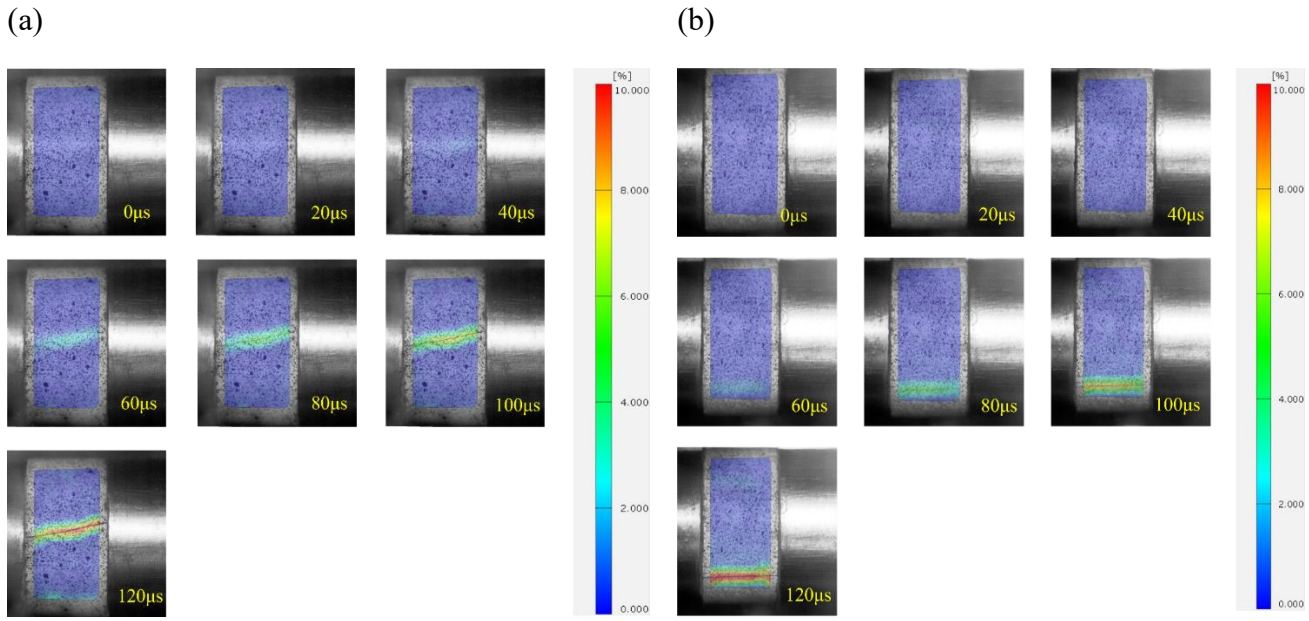



**Figure 10.** Dynamic dissipated energy of different impact pressure and OSP contents. **(a)** Impact pressure; **(b)** OSP content.

### *3.3. Failure pattern*

Figure 11 illustrates the failure process of specimens with different OSP contents under an impact pressure of 0.45 MPa. As illustrated in Figure 11a, the initial time is defined as the time at which the test block does not deform. At a time of 20 μs, the test block moves to the right as a whole, and the test block itself does not produce strain. Evidence indicates that the incident rod is subjected to impact at this juncture, initially coming into contact with a smear of Vaseline on the end face of the test block. At this stage, the force has not yet been applied to the test block. At 40 μs, it can be seen that the middle of the test block begins to produce small strain. At this time, the test block began to be impacted, and cracks were generated. At 120 μs, the initial micro-cracks develop into obvious cracks, which run through the two ends of the test block. After processing and analysis, it can be found that the approximate time from impact to damage of the test block is 120 μs.



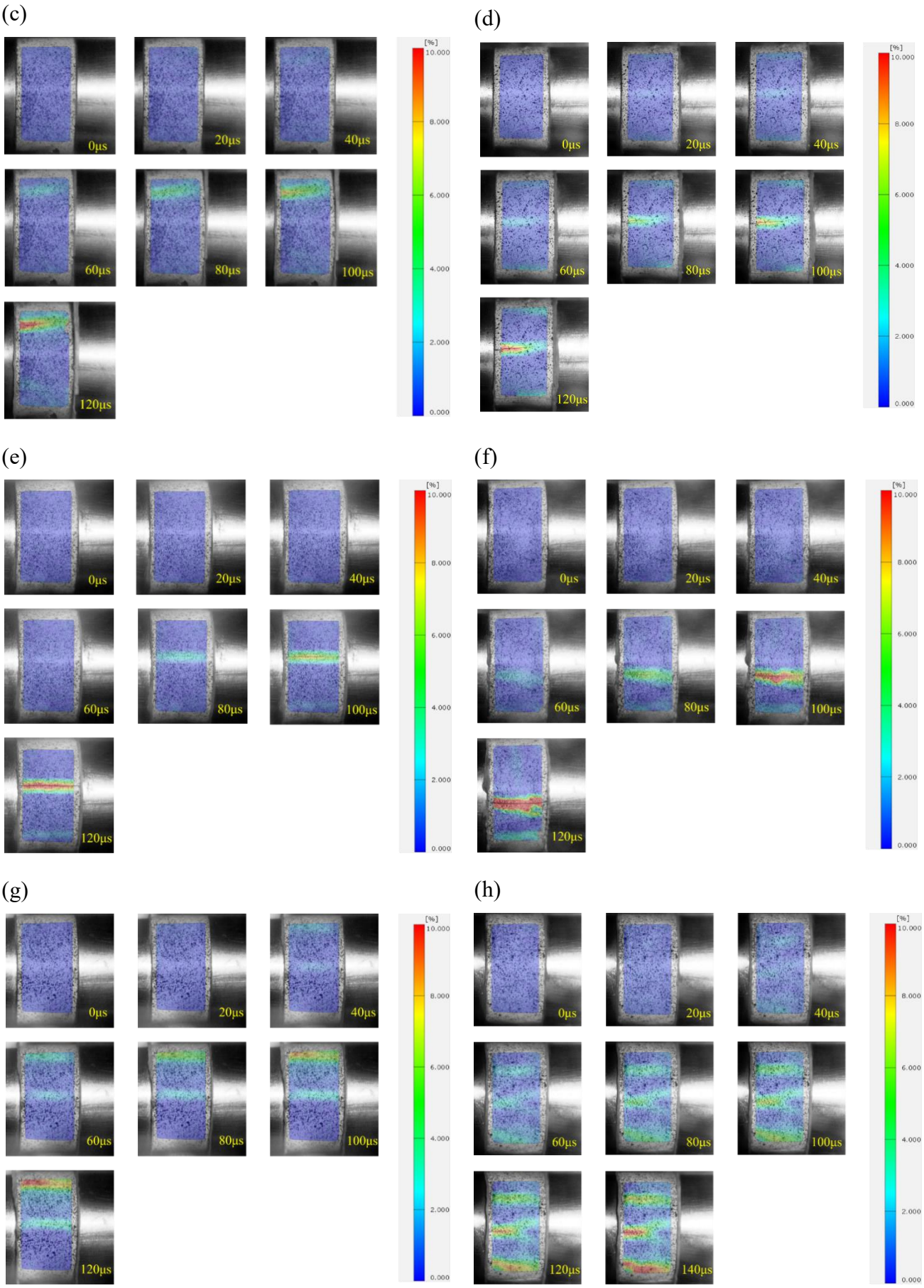



**Figure 11.** The change of real-time strain field of specimens with different OSP contents. **(a)** 0%; **(b)** 10%; **(c)** 20%; **(d)** 30%; **(e)** 40%; **(f)** 60%; **(g)** 80%; **(h)** 90%.

Figure 12 illustrates the failure morphologies of specimens with different OSP contents subjected to varying impact pressures. Both OSP content and impact pressure exert considerable influence on the failure characteristics of the geopolymer blocks. As the impact pressure rises, the degree of specimen pulverization intensifies, and the resulting fragments become progressively finer. This is attributable to the fact that higher impact pressure accelerates the striker velocity, thereby increasing the kinetic energy imparted to the specimen; consequently, greater impact energy leads to more severe damage. When the OSP content remains below 80 %, the extent of damage gradually diminishes with increasing OSP proportion. However, at a substitution level of 90 %, the degree of fragmentation increases notably. This behaviour is closely linked to the mechanical performance of the material. For OSP replacements below 80 %, the compressive strength initially increases and then decreases, but the overall variation stays within a margin of 10 %. However, at 90 % OSP content, the compressive strength decreases rapidly, with a reduction reaching up to 43 %, indicating that the material could not sustain the applied load adequately. Consequently, the extent of damage became more pronounced under the same impact pressure.

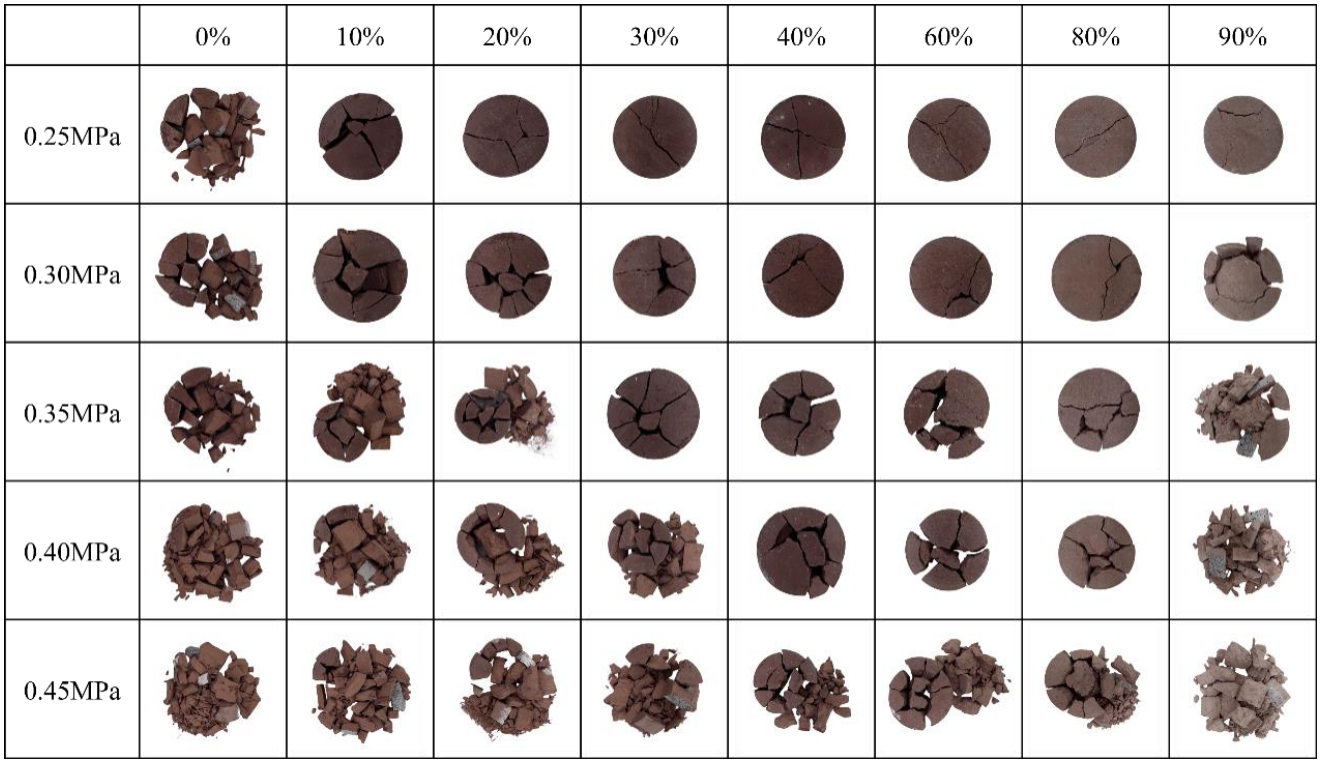



**Figure 12.** The failure diagram of the test specimens with different OSP contents under different impact pressure.

This research has promoted the development of smart and sustainable construction. The use of OSP as a replacement for metakaolin provides a method for recycling aquaculture solid waste, reducing the demand for raw materials and supporting low-carbon construction. The dynamic compressive strength, elastic modulus, and dissipated energy obtained from SHPB tests offer essential parameters for the seismic and impact resistance design of resilient infrastructure. In addition, the combination of high-speed photography and DIC analysis enables a digitally enabled assessment of material performance by capturing the real-time strain field and damage evolution. This provides data support and a reference basis for smart construction.

## 4. Conclusion

The influence of OSP substitution rates on the dynamic compressive behaviour of metakaolin-based geopolymer was investigated. All experiments were performed using the SHPB testing system, while high-speed cameras were employed to document the evolution of specimen damage throughout impact loading. Based on the experimental data, the dynamic compressive strength, dissipated energy, and failure patterns of geopolymer specimens with varying OSP contents were analyzed. The primary conclusions of this study are as follows.

(1) Incorporating OSP influences the compressive performance of metakaolin-based geopolymer. As the OSP proportion increases, both compressive strength and elastic modulus exhibit a rise and then a subsequent decline. The addition of OSP affects the energy absorption behaviour of metakaolin-based geopolymer. Under a fixed impact pressure, the dissipated energy of the specimens initially decreases and then increases with rising OSP content.

(2) The incorporation of OSP affected the fracture characteristics of metakaolin-based geopolymer. When the OSP replacement rate was less than 80%, the degree of damage gradually decreased as the OSP proportion increased. When the OSP replacement rate reached 90%, the degree of damage increased significantly.

(3) Impact pressure has a significant effect on OSP-modified metakaolin-based geopolymer. With increasing impact pressure, the compressive strength, elastic modulus, and dissipated energy all increase, accompanied by a higher degree of fragmentation upon specimen failure.

(4) The optimal OSP content of 20% was determined based on the dynamic compressive strength, elastic modulus, and dissipated energy. Geopolymers with a 20% OSP content exhibit excellent dynamic mechanical properties under various impact pressures. Selecting this optimal content provides a basis for structural design and safety assessments, particularly for seismic-resistant and protective structures.

In this study, the tested material was a metakaolin-based geopolymer paste in which OSP partially replaces metakaolin, and no coarse or fine aggregates were incorporated. The effect of OSP, as a calcium-containing additive, on the dynamic compression behavior of geopolymer cementitious materials was primarily analyzed. This study provides fundamental data for analyzing OSP-modified binder behavior under impact loading. In future research, aggregates and the ITZ will be incorporated, and the effects of carbonation and durability will be analyzed to better evaluate engineering applications.

## Data availability statement

No supplementary or additional data were generated in this study.

## Declaration of generative AI and AI-assisted technologies

The authors did not use generative AI or AI-assisted technologies in the writing of this manuscript.

## Acknowledgments

This study has no related funding.

## Authors' contribution

Conceptualization, L.F.; data curation, Z.L., Y.Z. and B.L.; formal analysis, P.G.; funding acquisition, L.F.; investigation, Z.L.; methodology, L.H. and B.L.; validation, P.G.; visualization, Y.Z.; writing—original draft, P.G.; writing—review and editing, L.F. All authors have read and agreed to the published version of the manuscript.

## Conflicts of interest

The authors declare no conflicts of interest.

## References

[1] Matsimbe J, Dinka M, Olukanni D, Musonda I. Geopolymer: a systematic review of methodologies. *Materials* 2022, 15(19):6852.

[2] Liew YM, Heah CY, Li LY, Jaya N, Abdullah MMA, *et al*. Formation of one-part-mixing geopolymers and geopolymer ceramics from geopolymer powder. *Constr. Build. Mater*. 2017, 156:9–18.

[3] Zaidi FHA, Ahmad R, Abdullah MMA, Abd Rahim SZ, Yahya Z, *et al*. Geopolymer as underwater concreting material: a review. *Constr. Build. Mater*. 2021, 291:123276.

[4] Zhang H, Jia TC, Sarker PK, Chen W, Wang Q, *et al*. Effect of fibre addition on the static and dynamic compressive properties of ambient-cured geopolymer concrete. *J. Build. Eng.* 2022, 58:104991.

[5] Chen C, Zhang X, Hao H. Dynamic tensile properties of geopolymer concrete and fibre reinforced geopolymer concrete. *Constr. Build. Mater*. 2023, 393:132159.

[6] Pan H, Xie Z, Chen G, Su J, Zhuo K, *et al*. Dynamic compressive behavior of high-strength engineered geopolymer composites. *J. Build. Eng*. 2023, 80:108036.

[7] Khan MZN, Hao Y, Hao H, Shaikh FUA. Mechanical properties and behaviour of high-strength plain and hybrid-fiber reinforced geopolymer composites under dynamic splitting tension. *Cem. Concr. Compos.* 2019, 104:103343.

[8] Li Z, Chen W, Yin Z, Ahmed M, Hao H. Lightweight ambient-cured geopolymer composite with expanded clay: quasi-static and dynamic properties. *Constr. Build. Mater.* 2024, 423:135800.

[9] Zhong W, Fan L, Zhang Y. Experimental research on the dynamic compressive properties of lightweight slag based geopolymer. *Ceram. Int.* 2022, 48(14):20426–20437.

[10] Su H, Xu J, Ren W. Mechanical properties of geopolymer concrete exposed to dynamic compression under elevated temperatures. *Ceram. Int.* 2016, 42(3):3888–3898.

[11] Wang Y, Zhong H, Zhang M. Experimental study on static and dynamic properties of fly ash-slag based strain hardening geopolymer composites. *Cem. Concr. Compos*. 2022, 129:104481.

[12] Pham TM, Liu JL, Tran P, Pang VL, Shi F, *et al*. Dynamic compressive properties of lightweight rubberized geopolymer concrete. *Constr. Build. Mater*. 2020, 265:120753.

[13] Feng KN, Ruan D, Pan Z, Collins F, Bai Y, *et al*. Mechanical behavior of geopolymer concrete subjected to high strain rate compressive loadings. *Mater. Struct.* 2015, 48(3):671–681.

[14] Ling Y, Zhang X, Zou W, Feng C, Lai H, *et al*. Axial impact resistance of high-strength engineering geopolymer composites: effect of polyethylene fiber content and strain rate. *Buildings* 2024. 14(5):1438.

[15] Huang Z, Chen W, Hao H, Aurelio R, Li Z, *et al*. Test of dynamic mechanical properties of ambient-cured geopolymer concrete using split Hopkinson pressure bar. *J. Mater. Civ. Eng.* 2021, 34(2):04021440.

[16] Xiao S, Liao S, Zhong G, Guo Y, Lin J, *et al*. Dynamic properties of PVA short fiber reinforced low-calcium fly ash-slag geopolymer under an SHPB impact load. *J. Build. Eng.* 2021, 44:103220.

[17] Li Z, Chen W, Hao H, Khan MZN, Pham TM. Dynamic compressive properties of novel lightweight ambient-cured EPS geopolymer composite. *Constr. Build. Mater.* 2021, 273:122044.

[18] Shi X, Zhang Y, Arachchi EN, Su Y. Study on dynamic impact properties of hybrid PVA-steel fiber reinforced geopolymer mortar. *J. Sustainable Cem.-Based Mater*. 2025, 14(8):1626–1638.

[19] Kuang F, Sun J, Liu P, Ping L, Wang L, *et al*. Study on dynamic compressive properties and mesoscopic numerical simulation of fiber-reinforced rubber geopolymer mortar. *Constr. Build. Mater*. 2025, 463:139993.

[20] Hong YM, Choudhury SR. The substitution effect of the fine aggregate in concrete with oyster shell. *Materials* 2024, 17(24):6148.

[21] Wei ML, Wei W, Li Y, Liu L, Zhong F, *et al*. Maximizing the pozzolanic potential of superfine iron tailings for low-carbon stabilization: application of high-calcium geopolymer. *Resour. Conserv. Recycl.* 2023, 198:107198.

[22] Adufu YD, Sore SO, Nshimiyimana P, Ahouandjinou KD, Messan A, *et al*. Durability behaviors of calcined kaolin clay-based geopolymer concrete containing different calcium compounds and cured in ambient sub-Saharan climate. *Constr. Build. Mater.* 2025, 465:140195.

[23] Ariyadasa PW, Manalo AC, Lokuge W, Aravinthan V, Gerdes A, *et al*. Macro and microstructural evolution of low-calcium fly ash-based geopolymer mortar exposed to sulphuric acid corrosion. *Cem. Concr. Res.* 2024, 178:107436.

[24] Kucukgoncu H, Ozbayrak A. Microstructural analysis of low-calcium fly ash-based geopolymer concrete with different ratios of activator and binder under high temperatures. *Arab. J. Sci. Eng*. 2025, 50(11):8197–8223.

[25] Yip CK, Van Deventer JSJ. Microanalysis of calcium silicate hydrate gel formed within a geopolymeric binder. *J. Mater. Sci.* 2003, 38(18):3851–3860.

[26] Lee WKW, Van Deventer JSJ. Chemical interactions between siliceous aggregates and low-Ca alkali-activated cements. *Cem. Concr. Res.* 2007, 37(6):844–855.

[27] Yip CK, Provis JL, Lukey GC, Van Deventer JSJ. Carbonate mineral addition to metakaolin-based geopolymers. *Cem. Concr. Compos*. 2008, 30(10):979–985.

[28] Shi X, Zhu X, Gao Q, Lyu X, Wang Z, *et al*. Innovative methods for converting low-value construction waste powders into geopolymer: mechanical-biobased alkaline-excited coupling for activation. *J. Build. Eng*. 2025, 116:114712.

[29] Djobo YJN, Elimbi A, Manga JD, Li Ndjock IBD. Partial replacement of volcanic ash by bauxite and calcined oyster shell in the synthesis of volcanic ash-based geopolymers. *Constr. Build. Mater*. 2016, 113:673–681.

[30] Zhang G, Lee S, Han Y, Wang X. The effect of oyster shell powder on the high-temperature-properties of slag-ceramic powder-based geopolymer. *Materials* 2023, 16(10):3706.
[31] Nasaeng P, Wongsa A, Cheerarot R, Sata V, Chindaprasirt P. Strength enhancement of pumice-based geopolymer paste by incorporating recycled concrete and calcined oyster shell powders. *Case Stud. Constr. Mater.* 2022, 17:e01307.
[32] Xuan M, Cho HK, Wang X. Performance improvement of waste oyster-shell powder-cement binary system via carbonation curing. *J. Build. Eng.* 2023, 70:106336.
[33] Meng Y, Da B, Yu X, Chen D, Li Y. Study on mechanical properties and durability of geopolymer concrete with oyster shell aggregate. *Constr. Build. Mater.* 2025, 472:140926.
[34] Wu Y, Lu J, Zhao L, He W. Alkali-activated waste seashell binder material: mechanical properties, reaction mechanism and life cycle assessment. *Sustain. Chem. Pharm*. 2025, 48:102219.
[35] Oyebisi S, Alomayri T. Revolutionizing eco-friendly concrete: unleashing pulverized oyster shell and corncob ash as cement alternatives for sustainable building. *Constr. Build. Mater*. 2025, 484:141776.
[36] Chen H, Li L, Lai Z, Kwan AKH, Chen P, *et al*. Effects of crushed oyster shell on strength and durability of marine concrete containing fly ash and blastfurnace slag. *Mater. Sci.-Medzg*. 2019, 25(1):97–107.
[37] Geferson OOJ, Desire BBP, Serge EJ, Odogu AN, Nsami NJ, *et al*. Sustainable and cleaner production of a porous geopolymer support based on metakaolin and natural calcium oxide. *J. Build. Eng*. 2024, 96:110638.
[38] Ziada M, Tanyildizi H, Uysal M. The influence of carbon nanotube on underwater geopolymer paste based on metakaolin and slag. *Constr. Build. Mater*. 2024, 414:135047.
[39] Su J, Mao J, Zhou B, Zhang W, Wang L, *et al*. Dynamic compressive mechanical properties of fibre-reinforced geopolymer concrete. *Case Stud. Constr. Mater.* 2025, 22:e04268.
[40] Hao Y, Hao H, Li Z. Influence of end friction confinement on impact tests of concrete material at high strain rate. *Int. J. Impact Eng.* 2013, 60:82–106.
[41] Zhou Z, Lu J, Cai X, Rui Y. Influence of interface morphology on dynamic behavior and energy dissipation of bi-material discs. *Trans. Nonferrous Met. Soc. China* 2022, 32(7):2339–2352.
[42] Fan L, Chen D, Zhong W, Zhang Y. Influence of interface inclination angle and load impact velocity on dynamic splitting tensile behavior and dissipated energy of geopolymer-concrete composites. *Constr. Build. Mater.* 2023, 403:133112.
[43] Ren J, Acarturk BC, Dowdy ND, Srubar III WV. The effects of calcium carbonate on sodium metasilicate-activated metakaolin-based geopolymer pastes. *Constr. Build. Mater.* 2024, 448:138218.
[44] Gai W, Dai F, He B, Zhou C, Wei M, *et al*. Influence of GGBFS and alkali activators on macro-mechanical performance and micro-fracture mechanisms of geopolymer concrete in split Hopkinson pressure bar tests. *Constr. Build. Mater.* 2024, 434:136736.